Check for updates

Laser & Photonics Reviews

LASER & PHOTONICS REVIEWS

www.lpr-journal.org

RESEARCH ARTICLE OPEN ACCESS

Wavefront Shaping for Optimal Extinction of Focused Light by Individual Nanoscatterers

Nick Feldman[1,2] | Joris Pals[1] | Arie J. den Boef[2,3,4] | F. Javier García de Abajo[5,6] | Lyubov V. Amitonova[2,3] | A. Femius Koenderink[1]

[1]Department of Information in Matter and Center for Nanophotonics, AMOLF, Amsterdam, the Netherlands | [2]Advanced Research Center for Nanolithography (ARCNL), Amsterdam, the Netherlands | [3]Department of Physics and Astronomy, and LaserLaB, Vrije Universiteit, Amsterdam, the Netherlands | [4]ASML Netherlands B.V., Veldhoven, the Netherlands | [5]ICFO-Institut de Ciencies Fotoniques, The Barcelona Institute of Science and Technology, Castelldefels, Barcelona, Spain | [6]ICREA-Institució Catalana de Recerca i Estudis Avançats, Barcelona, Spain

Correspondence: A. Femius Koenderink (f.koenderink@amolf.nl)

Received: 24 May 2026 | **Revised:** 30 August 2026 | **Accepted:** 28 September 2026

Keywords: extinction | nanophotonics | optics

ABSTRACT

Achieving complete optical extinction by small structures is key for applications such as photodetection and light harvesting, and constitutes a promising solution to the problem of efficient in-and-out coupling of light in nanophotonic devices. In this paper, we provide an innovative solution to this challenge by experimentally demonstrating optimal extinction by individual and arrayed scatterers separated from a planar reflecting surface, by shaping the wavefront of the input light. We fabricate and characterize planar particle arrays of sizes ranging from extended lattices to individual nanoparticles, separated from a planar, partially absorbing surface by a controlled distance. By optimizing the incident wavefront of a tightly focused light beam and the particle–surface separation, we achieve optimal coupling to a single nanoparticle-on-mirror structure. Comparison with theory shows that the optimum incident wavefronts correspond to the time-reversed emission profiles from the nanoscatterer in the presence of the planar reflector. Using these optimal illumination conditions, we demonstrate 70% extinction of a tightly focused beam by a single plasmonic nanoparticle, and up to 90% extinction in sub-wavelength 2×2 clusters of nanoparticles on a reflector. These results constitute a solid step toward a practical solution to the in-and-out light coupling problem in nanophotonics.

1 | Introduction

Optical extinction describes the fraction of energy that is removed from a light beam due to scattering and absorption by atoms, molecules, or material structures, and provides a quantitative metric for the strength of different light–matter coupling mechanisms. Extinction includes elastic scattering, which consists of the redirection of incident light caused by an obstacle, as well as absorption by a material. Strong optical extinction is desirable in applications such as high-efficiency solar cells [1], optical sensors [2], modulators [3], and anti-reflection structures [4]. This has raised an important question within the photonics community: how *complete* optical extinction can be achieved in designer materials. A hallmark example of complete optical extinction comes in the form of absorption by Salisbury screens [5, 6], in which a thin layer of resistive material is placed at a quarter wavelength from a back reflector. The essential physics of these Salisbury attenuators relies on in-phase superposition of incident and reflected light, which is therefore completely absorbed by the resistive sheet. Sparked by recent progress in the field of nanotechnology, Salisbury screens have been complemented by designer sub-wavelength spatially varying patterns to achieve perfect absorption in spectral regimes ranging from microwaves [7, 8] to near-infrared [9–12] and optical frequencies [13–15]. Such

This is an open access article under the terms of the Creative Commons Attribution License, which permits use, distribution and reproduction in any medium, provided the original work is properly cited.
© 2026 The Author(s). *Laser & Photonics Reviews* published by Wiley-VCH GmbH.

perfectly absorbing systems have also been connected to the notion of *coherent* perfect absorption [16, 17], leveraging light interference through coherent illumination by multiple waves.

In all the examples discussed thus far, extended thin films or spatially patterned surfaces are used as the extinction medium. A question that has intrigued the optics community for decades is how much extinction can be achieved from a finite collection of small particles or even single isolated nanoparticles. A crucial distinction is that, for infinitely extended surfaces illuminated by a plane wave under a fixed angle of incidence, there is just a single input and output channel (the input plane wave and its specular reflection), so that perfect absorption can be easily achieved by arranging for perfect destructive interference of scattering with the direct reflection in the single output port. For finite objects, extinction is also defined as the destructive interference of scattered light and the incident field. However, finite scattering objects scatter light into all wave-vector components (i.e., into many more channels than just the direct reflection of the incident plane wave). Consider the scenario of a single lossless and resonant nanoscatterer with dimensions much smaller than the light wavelength λ that is illuminated by an infinitely extended plane wave. Under these conditions, the nanoparticle can be described within the dipole approximation, and attenuation is quantified by the notion of extinction cross section C_{ext}. It can be shown [18] that the maximum achievable extinction cross section is given by

$$C_{\text{ext}} = \frac{3}{2\pi}\lambda^2. \tag{1}$$

Due to the lossless nature of the nanoparticle, extinction is fully caused by scattering losses. For lossy nanoparticles, the maximum absorption cross section occurs under the so-called critical coupling conditions [18–20], in which scattering and absorption losses are made equal. Beyond the dipole approximation, superscattering nano-objects have been proposed that can surpass the limit of Equation (1) by exploiting overlapping multipole resonances in subwavelength nanostructures [21].

Instead of plane-wave illumination, the coupling of incident light and a nanoparticle can be enhanced by tightly focusing the incident light to a diffraction-limited spot size. In this scenario, extinction is defined by the dimensionless fraction of power removed from the incident focus. Comparing the result of Equation (1) with the typical cross section of a tightly focused beam, which is of the order of $(\lambda/2)^2$, one concludes that a single nanoparticle can, in principle, attenuate a large fraction of a focused beam. Indeed, numerical work has shown that a single oscillating dipole positioned in a homogeneous medium can cause up to 100% extinction of a focused light beam [22]. On the experimental side, studies have reported high extinction contrasts by dipolar transitions in single quantum emitters [23–25]. In parallel, several studies on the interactions of focused light fields with two-level systems [22, 26–28] have argued that precise wavefront and polarization structuring of the incident focus is required to achieve an optimum coupling between excitation and scatterer, which would lead to a larger extinction. For instance, by illuminating a dipolar particle with a strongly focused directional dipole wave, the particle can theoretically cause perfect extinction of the incident focused light beam [22, 28]. This can be explained from the viewpoint of time reversal symmetry: a nanoparticle emitting light into a dipolar far-field pattern would be most efficiently excited by a time-reversed field that matches this dipolar pattern, and experiments have been proposed [27] that offer two-sided dipolar illumination schemes that cover the full 4π solid angle. By virtue of the optical theorem, which traditionally states that extinction of an object can be determined solely from its scattering in the forward direction, the argument can also be recast in the language of destructive interference: by maximizing the similarity between the radiation pattern and the wavefront of the direct beam, one maximizes destructive interference and hence extinction. More recently, theoretical works [28, 29] have shown that positioning a single nanoparticle at an optimum distance from a reflective substrate can cause perfect extinction of a focused light beam, assuming optimal structuring of the incident field over 2π incident angles. The mirror limits the scattered wave to 2π instead of 4π steradians, easing the challenge of optimally structuring the incident field. In a way, these studies provide a single-particle analogue to Salisbury screens, in which a single nanoscatterer replaces the thin resistive layer. The crucial distinction here is the number of available ports: in the extended Salisbury screen, the incident field can only be directly reflected or transmitted in the zero-order channel, whereas a single nanoparticle is allowed to scatter light into a continuous angular spectrum. Note that this distinction can be extended to the interference argument as well: While Salisbury screens are designed to cause complete destructive interference between the direct specular reflection caused by the back mirror (which is the outgoing part of the incident wave) and the specular reflection of the resistive sheet, the radiation pattern of the single nanoparticle-on-mirror system causes complete destructive interference with its time-reversed incident focus reflected by the back mirror. However, to the best of our knowledge, no experimental studies have been reported that investigate optimal extinction scenarios in single-particle-based Salisbury-screen platforms, nor examine how mode matching of the external illumination influences total extinction.

In this work, we study extinction in Salisbury-screen attenuators down to the single nanoparticle level and experimentally demonstrate that wavefront engineering of an incident focused beam leads to optimum extinction scenarios. The concept is schematically depicted in Figure 1a. A dipolar nanoparticle situated above a back reflector is excited by an externally applied, tightly focused incident field $\mathbf{E}_{\text{in}}$ and emits a scattered field $\mathbf{E}_{\text{scat}}$ into the far field, of which the scattered phase is shown in a polar plot. When the incident field is shaped such that it is phase conjugated (which is the monochromatic equivalent of time-reversal) with respect to the scattered field (i.e., $\mathbf{E}_{\text{in}} = \mathbf{E}^*_{\text{scat}}$), complete destructive interference can happen between the back-reflected incident field from the back reflector $\mathbf{E}_{\text{r}}$ and the scattered field of the nanoparticle $\mathbf{E}_{\text{scat}}$, which leads to an optimum extinction condition. As a starting point, we revisit the well-known perfect absorption phenomenon in extended particle arrays near Salisbury screens, after which we study how finite-size effects affect optimal extinction conditions when gradually reducing the array size all the way down to a single scattering nanoparticle. To this end, we have developed a high-numerical-aperture (NA) wavefront shaping protocol that allows us to precisely engineer wave vector components of a tightly focused beam and demonstrate that time reversal of the radiation patterns

18638899, 0, Downloaded from https://onlinelibrary.wiley.com/doi/10.1002/lpor.70232 by Centrum Voor Wiskunde En Info (Cwi), Wiley Online Library on [29/10/2026]. See the Terms and Conditions (https://onlinelibrary.wiley.com/terms-and-conditions) on Wiley Online Library for rules of use; OA articles are governed by the applicable Creative Commons License

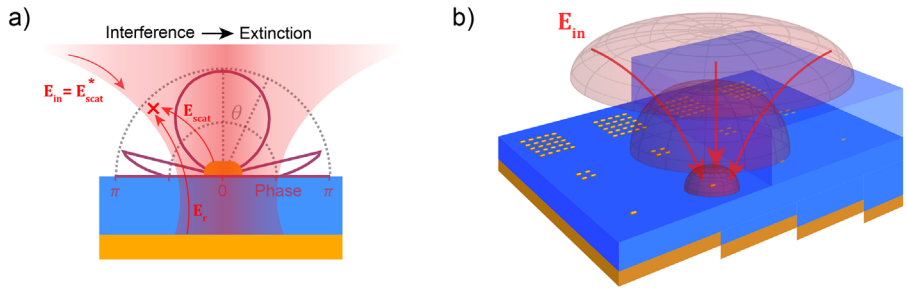


FIGURE 1 | Experimental concept and sample architecture. (a) An externally applied, tightly focused incident field $\mathbf{E}_{in}$ excites a dipolar nanoparticle-on-mirror system, after which the particle emits a scattered field $\mathbf{E}_{scat}$ into the far-field. When the incident field is shaped such that it corresponds to the phase-conjugated (time-reversed) scattered field ($\mathbf{E}_{in} = \mathbf{E}^*_{scat}$), complete destructive interference between the backreflected field $\mathbf{E}_r$ and the scattered field $\mathbf{E}_{scat}$ can happen, leading to an optimum extinction scenario. (b) We fabricate plasmonic nanoparticle arrays separated from a back reflector by a dielectric spacer layer of variable thickness. The sizes of the arrays are varied from extended lattices to finite-size patches, and single nanoscatterers.

of single nanoscatterers leads to optimum extinction conditions. Using this strategy, we demonstrate up to 70% extinction of focused light in single plasmonic nanoparticles, and 90% in sub-wavelength clusters of 2×2 particles on a reflector.

2 | Finite Size Effects

Figure 1b depicts the sample architecture used in our experiments. We fabricate plasmonic arrays of different sizes consisting of gold nanorods, ranging from effectively infinite arrays to finite-size patches containing a few nanoparticles and down to single nanoparticles. Specific nanofabrication procedures and parameters are discussed in the Methods section. In all designs, the length, width, and height of the nanorods are 100, 50, and 40 nm, respectively, and the arrays have a period of 200 nm. These values are in line with a recent literature study [15] and are chosen such that the dipolar resonances of the system are within the detection range of our experimental setup. Multiple copies of these arrays are patterned on a substrate, after which we deposit a dielectric SiO_2 spacer layer with a variable thickness ranging from roughly 200 to 640 nm in steps of 10 nm. The spacer layer is finally covered by a back reflector, yielding a nanoparticle-based Salisbury-screen platform. We also fabricate reflectors in the same plane as the nanoparticles, which allows us to accurately determine the variable spacer height by measuring the Fabry–Pérot etalon resonances in the resulting mirror–spacer–mirror regions that are immediately adjacent to the arrays and particles under test (see Supporting Information for details). Figure 2a–d shows scanning electron microscopy (SEM) images of typical arrays with varying sizes, which are taken before deposition of the dielectric graded layer and mirror.

To probe the extinction properties of these particle array patches, we acquire reflection spectra as a function of spacer height while gradually reducing the array size to, ultimately, a single nanoscatterer. Since the reflectivity of a 50 nm bare gold film is approximately 0.95, the back mirror eliminates almost all transmission channels in the sample. We thereby determine particle extinction by computing 1 minus particle reflection. We remind the reader that the transition from extended particle arrays to finite arrays or a single particle is accompanied by an increase in the number of available scattering channels under plane-wave illumination at a fixed incidence angle. Specifically, an extended array couples only to the specular reflection channel, whereas finite arrays and single particles scatter into a continuous high-NA angular spectrum. This difference in available scattering channels imposes different wave vector conditions on the illumination to reach optimal extinction in the respective structure under test. Therefore, our strategy to move from array measurements toward single-particle extinction measurements is as follows. We start by measuring reflection spectra of very large 100×100 μm^2 arrays using near-normal illumination, revisiting literature results [15]. On this effectively infinite array, we then gradually switch the illumination conditions from near-normal incidence to high-NA tight focusing, which is required for single-nanoparticle optimal extinction studies, and investigate how the measured extinction depends on the NA of the incident focus. The high-NA focused illumination conditions are then used to probe finite array size effects. In all measurements, the polarization state of the incident beam is aligned parallel to the long axis of the nanorods. Details on the experimental setup and data acquisition parameters can be found in the Supporting Information.

We first turn our attention to reflectivity spectra acquired on the 100×100 μm^2 array with a pitch of 200 nm, as shown in Figure 2e. These arrays are illuminated by a low effective NA of 0.1, softly focused onto the center of the array. Every vertical slice in this image corresponds to a reflection spectrum acquired on a different array realization, separated by a different spacer thickness from the back reflector. It has been shown in an earlier work [15] that such *metasurface etalons* result in pairs of singular points of zero reflection/perfect absorption in the 2D parameter space spanned by the spacer height and the light wavelength, which are associated with topological phase singularities. These perfect absorption conditions originate from a hybridization of array plasmon resonances and Fabry—Pérot etalon resonances. From the spectra of Figure 2e, we clearly observe such a singular pair of (nearly) null reflection points between spacer heights of 300 and 500 nm, approaching bright lines of near unity reflection corresponding to the etalon resonance conditions. These singular pairs are repeated indefinitely (assuming infinitely extended arrays illuminated at normal incidence) for higher spacer heights that lie outside the range of our fabricated sample. The small but finite wave vector spread that is associated with the incident NA results in a small residual reflection at the singular points.

18638899, 0, Downloaded from https://onlinelibrary.wiley.com/doi/10.1002/lpor.72032 by Centrum Voor Wiskunde En Info (Cwi), Wiley Online Library on [29/10/2026]. See the Terms and Conditions (https://onlinelibrary.wiley.com/terms-and-conditions) on Wiley Online Library for rules of use; OA articles are governed by the applicable Creative Commons License

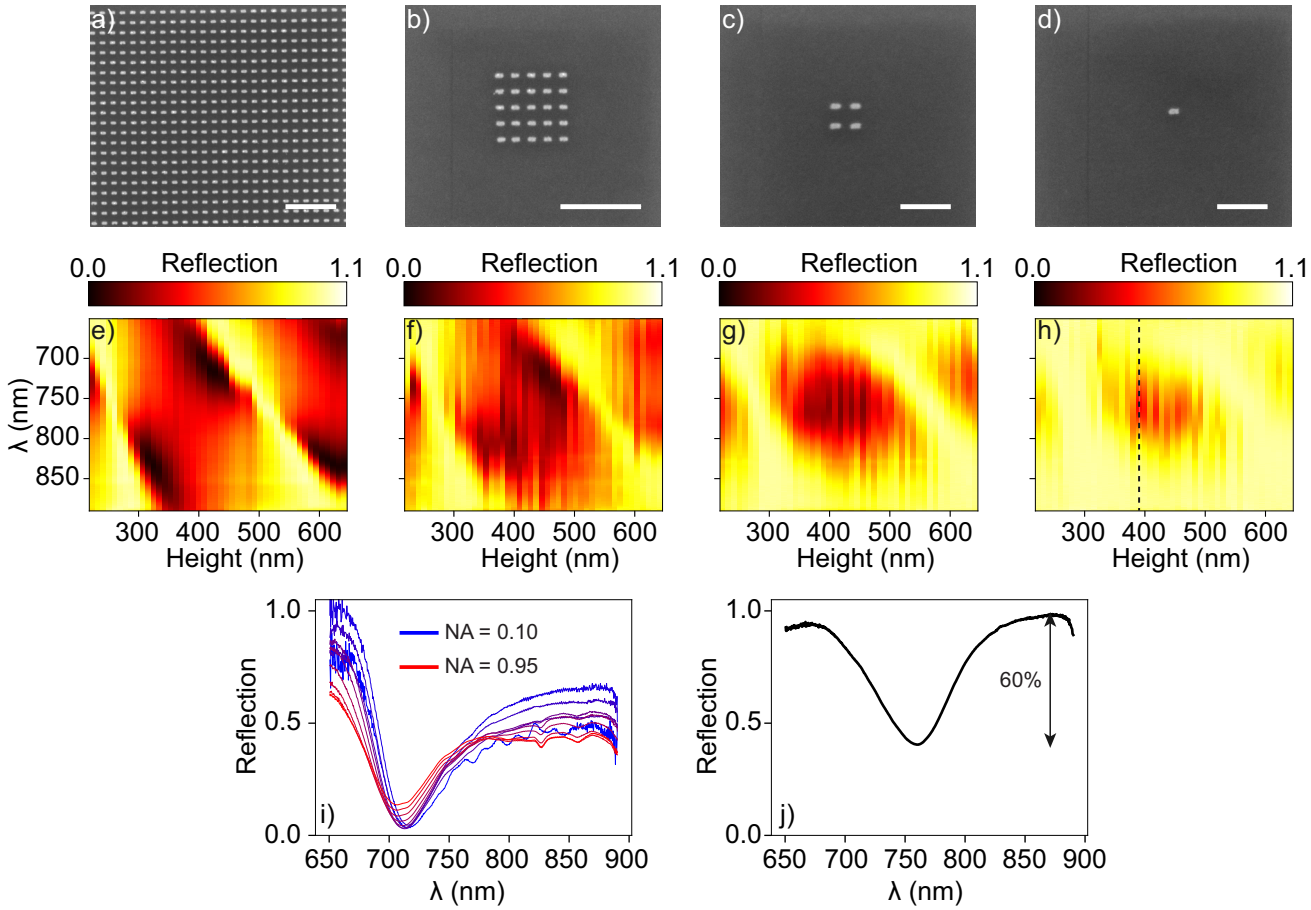


FIGURE 2 | Optimal extinction in finite-size particle arrays on Salisbury screens. SEM images of arrays fabricated on a variable spacer height with an array size of (a) 100×100 μm^2; (b) 5×5 particles; (c) 2×2 particles and (d) a single particle. Scale bars correspond to 1 μm in panels (a) and (b), and 500 nm in (c) and (d). Panels (e)–(h) show experimentally measured reflection spectra as a function of spacer height for the arrays in (a)–(d), respectively. The spectra of panel (e) are acquired using a low NA = 0.1 softly focused illumination, while the spectra of panels (f)–(h) are obtained using an NA=0.95 tightly focused beam, both focused onto the center of the arrays. (i) Reflection spectra captured on a 100×100 μm^2 array separated by 427 nm from the back reflector, for different numerical apertures (NAs) in the 0.1–0.95 range. (j) Reflection spectrum of a single nanoparticle separated from the back reflector by 389 nm, which corresponds to the sliced spectrum of panel (h) as indicated by the dashed line.

To visualize the effect of incident NA on the extinction properties of such a 100×100 μm^2 metasurface etalon around the normal-incidence perfect absorption condition, we acquire reflection spectra at a constant spacer height of 427 nm while gradually increasing the NA of the incident focus from 0.1 to 0.95, which is the maximum NA of our microscope objective. We control the incident NA by placing an iris in the conjugate back-focal-plane (Supporting Information), where different iris aperture sizes correspond to different NA values. A gradual increase in residual reflection is observed when increasing the NA, highlighting the specificity of the singular points to incident wave vectors. Using the high-NA focused illumination, we then progress to finite array patches, again acquiring reflection spectra on a range of different realizations of arrays with sizes of just 5×5 particles, 2×2 particles, and a single particle as a function of spacer height, and show the results in Figure 2f–h. We observe that, as the array decreases in size, the pair of singular points gradually vanishes into a single broad feature corresponding to the plasmon resonance of the single particle. This highlights the importance of extended lattices in the creation of topological singular points in the 2D parameter space. The minimum reflection value slowly increases as well for smaller array sizes. Nevertheless, a single plasmonic nanoparticle situated at the optimal height from the back reflector still causes a substantial extinction of almost 60%, as highlighted by the single particle reflection spectrum in Figure 2j. This specific reflection spectrum is a vertical slice of Figure 2h that corresponds to optimum (maximum) extinction, and, importantly, this extinction value is achieved without a particular tailoring of the incident wavefront to the radiation pattern of a dipole. The only shaping of the incident wave that evidently matters is to place the antenna in a field maximum of the standing wave formed by the incident focus and its reflection off the back reflector.

3 | Wavefront Optimization Protocol

In this section, we describe how the extinction by single nanoparticles can be further optimized by tailoring the incident wavefronts. For this, we band-pass filter the illumination wavelength at 760 nm with a bandwidth of 10 nm, such that the excitation spectrally overlaps with the maximum extinction value as measured in Figure 2h. We set the polarization state of the incident beam to be *y*-polarized and align the long axis

18638899, 0, Downloaded from https://onlinelibrary.wiley.com/doi/10.1002/lpor.72032 by Centrum Voor Wiskunde En Info (Cwi), Wiley Online Library on [29/10/2026]. See the Terms and Conditions (https://onlinelibrary.wiley.com/terms-and-conditions) on Wiley Online Library for rules of use; OA articles are governed by the applicable Creative Commons License

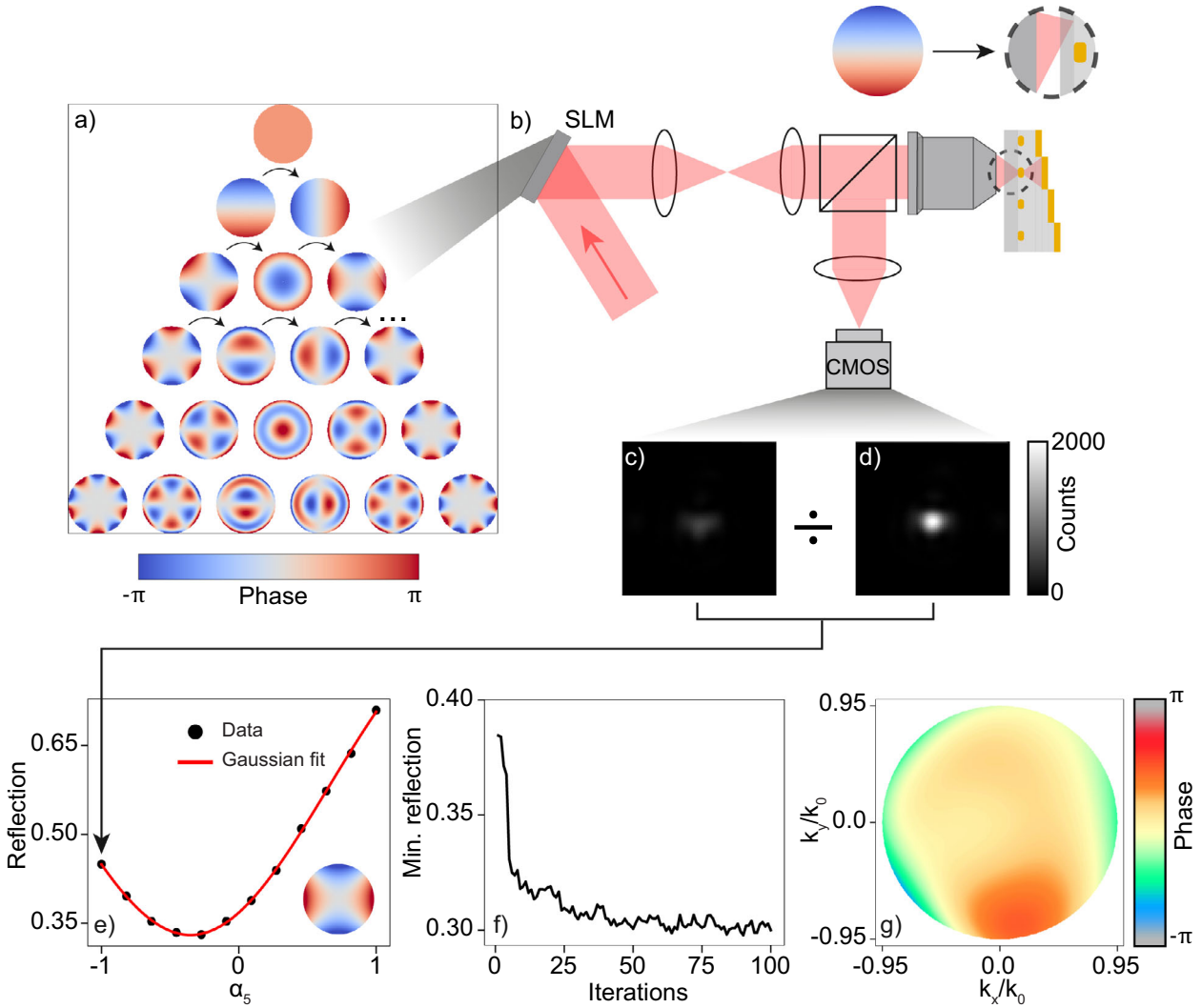


FIGURE 3 | Experimental wavefront optimization routine for an individual scatterer. (a) Individual phase contributions described by Zernike polynomials that are linearly superimposed and projected by a spatial light modulator. The procedure to optimize coefficients to obtain optimum extinction is described in the main text. (b) The phase patterns are relay imaged onto the back-focal-plane of the microscope objective, which focuses the incident wavefronts onto single nanoparticles. An additional phase-ramp pattern applied on the SLM shifts the focus either on or off a single nanoparticle. The back-reflected point-spread function is captured on a CMOS detector, with typical point-spread functions both on and off the single nanoparticle shown in panels (c) and (d), respectively. From these point-spread functions, a single particle reflection value can be determined, and plotted versus weighting coefficient α_n of the relevant Zernike polynomial. In panel (e), exemplary data for α_5 are shown, where the black dots denote measured data and the red line a Gaussian fit. (f) Minimum reflection values as a function of all iterations in the optimization. (g) Resulting wavefront after applying the optimization procedure. All data shown in this figure are measured on a single nanoparticle separated from the mirror by 389 nm.

of the nanorods to be parallel to this direction in order to excite the longitudinal plasmon resonance. The transverse dipole mode in the nanorod, whose resonance wavelength lies outside the detection window of our setup, emits an equivalent far-field emission pattern to the longitudinal mode up to a 90° rotation. We therefore expect the optimum wavefront for the two polarization channels to be identical. The experimental wavefront optimization workflow is depicted in Figure 3 for a single nanorod positioned at the optimum spacer height from the mirror (389 nm), which is defined as the height at which maximum extinction in reflectivity is obtained with an unshaped tightly focused beam. The optimization algorithm is based on an iterative protocol commonly used within the wavefront shaping community [30], and allows for a more intuitive interpretation of optimization results than more sophisticated strategies such as the steepest-gradient descent method, although the latter might be an option for future implementations. Here, we rely on a set of Zernike polynomials [31] as depicted in Figure 3a, which are widely used in the optics community (e.g., in phase retrieval experiments [32] and in the characterization of aberrations in imaging systems [33]). Zernike polynomials $Z_n(k_x, k_y)$ form a complete and orthogonal set of functions on the unit disk, which allows any wavefront $\varphi(k_x, k_y)$ to be decomposed as a linear combination of those polynomials

$$\varphi(k_x, k_y) = \sum_n \alpha_n Z_n(k_x, k_y), \tag{2}$$

where α_n are the corresponding expansion coefficients. Finding the optimum wavefront that maximizes the extinction can thus

18638899, 0, Downloaded from https://onlinelibrary.wiley.com/doi/10.1002/lpor.72032 by Centrum Voor Wiskunde En Info (Cwi), Wiley Online Library on [29/10/2026]. See the Terms and Conditions (https://onlinelibrary.wiley.com/terms-and-conditions) on Wiley Online Library for rules of use; OA articles are governed by the applicable Creative Commons License

be conveniently rephrased as finding the optimum contribution of each Zernike polynomial, thereby retrieving the optimum expansion coefficients α_n. To this end, we project a linear combination of Zernike polynomials on a spatial light modulator (SLM) that we accumulate sequentially, that is, by adding order after order and optimizing just the coefficient of the highest order term as we add it, as depicted in Figure 3b. This pattern is relay imaged onto the back-focal-plane (BFP) of the microscope objective, thereby modulating the phase of incident wave vectors, while the objective focuses the incident light onto a single nanoscatterer. To obtain the optimum expansion coefficient for each n, we measure single particle reflectance values for a range of α_n by measuring reflected point-spread-functions (PSFs) of the focus both on and off (i.e., away from) a particle, continuously referencing these two measurements to each other to determine the extinction. Switching between on- and off-particle excitation is achieved by projecting an additional phase-ramp pattern on top of the Zernike expansion, which causes a shift of the focus in the sample plane. This procedure avoids any mechanical sample movements and, hence, potential drifts during the measurement. Example PSFs of a focus corresponding to an extreme value of α_n (with $n = 5$) both on and off a single nanoparticle are shown in Figure 3c and Figure 3d, respectively. The corresponding measured reflection values as a function of α_5 are shown in Figure 3e as black data points, from which a clear minimum in reflection can be observed. Fitting the data with a Gaussian function, depicted by the red solid line in Figure 3e, allows us to identify the optimum expansion coefficient α_n, after which the next Zernike polynomial is projected on the SLM. This process is repeated for 20 Zernike polynomials (excluding Z_0, which corresponds to an arbitrary phase offset) according to the sequence depicted in Figure 3a. At the end of this process, we restart the optimization at Z_1 and repeat this cycle of optimization five times to ensure convergence. The minimum reflectance value for all iterations is shown in Figure 3f, showing a convergent behavior. It can be seen that an additional 8% in extinction is achieved through illumination with an optimized wavefront with respect to an unmodulated wavefront, reaching nearly 70% extinction by a single nanoparticle. The resulting optimum wavefront that is projected onto the SLM after completing the optimization routine is shown in Figure 3g. We confirmed that convergence is reached for all spacer heights by applying the optimization protocol to 2×2 clusters of nanoparticles separated from the mirror by 202, 305, 389, 529, and 641 nm, of which the results are shown in the Supporting Information. For a height of 389 nm, we observe that a sub-wavelength cluster of 2×2 nanoparticles is able to cause > 90% extinction of focused light.

It is important to note that small alignment imperfections cause additional minute aberrations in the excitation path of the setup. An unmodulated phase pattern (flat phase) projected onto the SLM therefore does not correspond to an actual flat phase profile in the BFP of the microscope objective. The optimization routine thus optimizes for both the matching of scattered wavefronts from a single nanoparticle-on-mirror, and for the removal of these extra aberrations in the setup. The optimal wavefront shown in Figure 3g shows the combination of these two effects, which explains the asymmetric features present in the wavefront.

4 | Time Reversal of Scattered Wavefronts

We now more closely analyze the resulting optimized wavefronts as extracted from the optimization workflow described in the previous section, and qualitatively argue that the resulting incident wavefronts are correlated to time-reversed scattered wavefronts from a nanoparticle-on-mirror system. To gain insights into the scattering behavior of a nanoparticle on a mirror, we perform analytical calculations in which we model the nanoparticles as dipolar scatterers in a layered system using the Green function of the stratified system [34] and corresponding modeling parameters as discussed in the Methods section. For this, we utilize the Python package "PyRAMIDS", which will shortly be released as open-source software through a separate publication. We calculate the scattered intensity and phase from a single dipole separated by a varying distance from a gold back reflector, and plot the resulting polar emission patterns in Figure 4. Specifically, the dipole is oriented in the y-direction, which is aligned parallel to the long axis of the plasmonic nanorods in the wavefront shaping experiments. Here, we choose spacer height values of 202, 305, 389, 529, and 641 nm, and visualize both scattered intensity and phase as black and red curves, respectively. From this figure, we can observe strong variations in dipolar emission as a function of spacer height. The variation in scattered intensity is the fundamental reason why only a small range of spacer heights causes optimal extinction, as observed in Figure 2h. For these optimal heights, a nanoscatterer can most efficiently scatter light into a high-NA angular far-field spectrum, as shown, for instance, in the emission pattern of Figure 4c, which can therefore efficiently interfere with a high-NA focused illumination, causing optimal extinction. The variation in scattered phase indicates that a different optimal incident wavefront is required for each spacer height to cause optimal extinction. We investigate this height-dependent variation in the optimum wavefront by inspecting the optimum wavefronts retrieved from the optimization measurements performed on particles positioned on different spacer heights. For experimental convenience, we perform the optimization on the 2×2 clusters of nanoparticles, but note that, due to the symmetry and sub-wavelength dimensions of these clusters, the far-field emission characteristics are nearly identical to those of single nanorods, up to an overall increase in scattered field amplitude. Therefore, we argue that the optimum wavefronts retrieved from 2×2 particle clusters and single particles would be essentially identical.

To decouple the effects of aberrations in the setup from the relevant spacer height-dependent variations in scattered wavefronts, we inspect differences in optimum wavefronts relative to a reference wavefront optimized for a constant spacer height. We show differential optimized wavefronts in Figure 5a–d for spacer heights of 305, 389, 529, and 641 nm, respectively, all referenced to the optimum wavefront for the spacer height of 202 nm. We further subtract an arbitrary phase offset from all differential wavefront patterns, such that the center of Fourier space corresponds to a differential phase of 0 radians. The resulting relative phase profiles show a higher degree of symmetry than the raw optimized wavefronts, indicating that the effect of static aberrations is indeed removed after referencing. We attribute the remaining minute asymmetries to a slight tilt of the sample with respect to the objective. Striking differences are

18638899, 0, Downloaded from https://onlinelibrary.wiley.com/doi/10.1002/lpor.72032 by Centrum Voor Wiskunde En Info (Cwi), Wiley Online Library on [29/10/2026]. See the Terms and Conditions (https://onlinelibrary.wiley.com/terms-and-conditions) on Wiley Online Library for rules of use; OA articles are governed by the applicable Creative Commons License

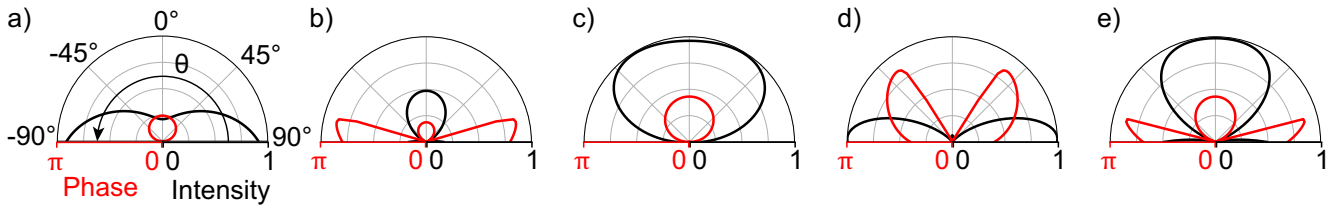


FIGURE 4 | Theoretical emission patterns from a dipole on mirror. Scattered intensity and phase of a *y*-oriented dipolar scatterer on a mirror are indicated as black and red solid curves respectively. The spacer height is varied in each panel as (a) 202; (b) 305; (c) 389; (d) 529, and (e) 641 nm.

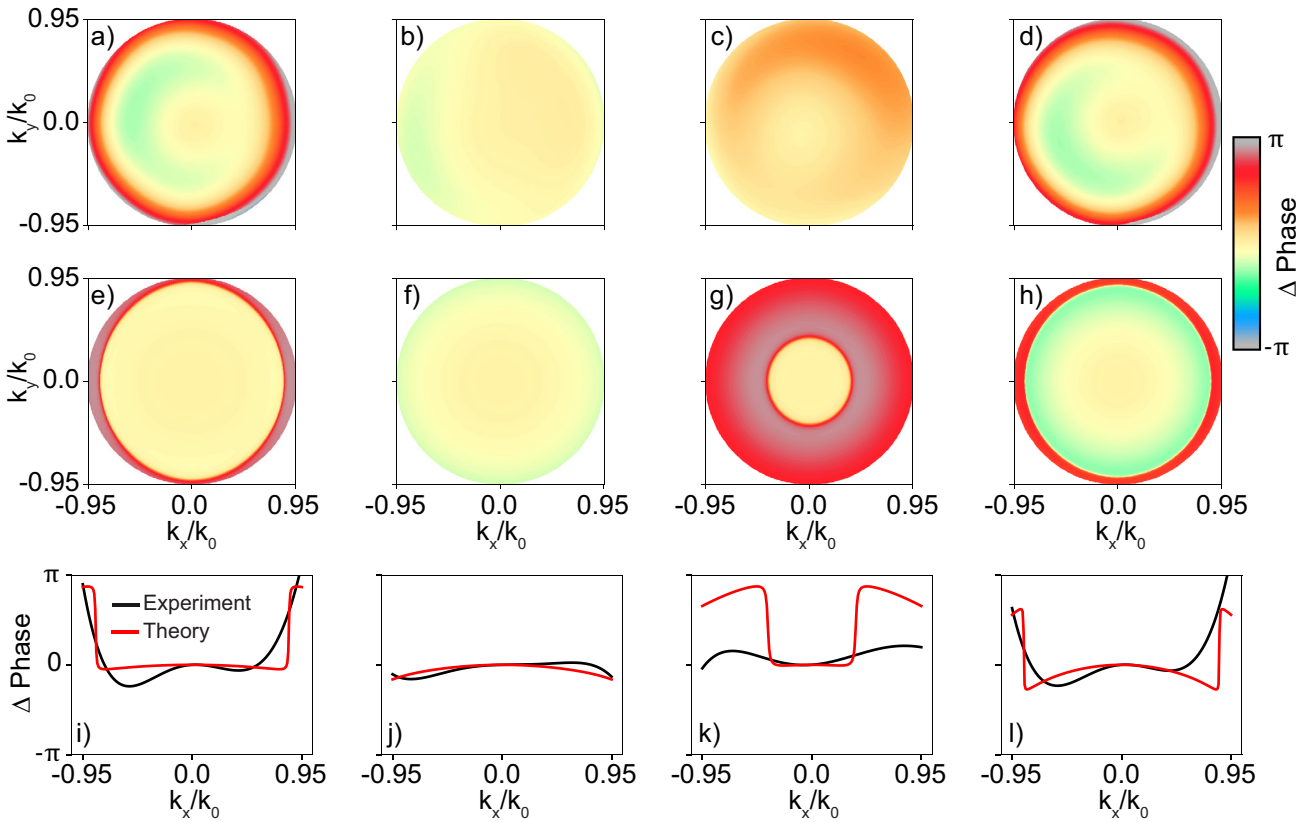


FIGURE 5 | Differential phase profiles versus spacer height, (a)–(d) Differential phase profiles extracted from the experimental optimization procedure, where the optimum phase profile at a spacer height of 202 nm is subtracted from the optimum phase profile at a spacer height of (a) 305, (b) 389, (c) 529, and (d) 641 nm. All wavefronts are optimized for a cluster of 2×2 particles. (e)–(h) Theoretical differential phase patterns of the scattered wavefront of a dipole on a mirror. The same height conditions as in panels (a)–(d) are used. (i)–(l) Line cuts of panels (a)–(h) through the $k_y/k_0 = 0$ axis, where the black and red curves denote experimentally optimized wavefronts and theoretical differential wavefronts, respectively. An arbitrary phase offset is subtracted from all differential phase profiles, such that the center in Fourier space corresponds to a differential phase of 0 radians.

again observed for the optimized wavefronts as a function of spacer height. We note especially that the differential wavefronts shown in Figure 5a,d show interesting features, where a rapid relative phase variation shows up at high excitation angles. To draw a qualitative comparison between the expected dipolar scattered wavefronts, we show theoretical far-field scattering calculations of relative phase profiles in Fourier space from a dipole-on-mirror system in Figure 5e–h, using again the exact same height parameters as were chosen in the experiment. We observe qualitative similarities between the theoretical scattered differential wavefronts and the experimental optimized differential wavefronts. To draw a closer comparison, we plot line cuts of the Fourier space images through the $k_y/k_0 = 0$ axis in Figure 5i–l, and show experimental and theoretical relative wavefronts as black and red curves, respectively. Note that the curvatures of all relative optimized wavefronts qualitatively agree with the theoretical scattered relative phase profiles.

Quantitative discrepancies between theoretical and optimized wavefronts remain, which we attribute to the following main causes. First of all, possible steep wavefront gradients in the optimum wavefront, which are described by the higher-order Zernike polynomials, are only reconstructed approximately due to the finite number of lower-order Zernike polynomials present

18638899, 0, Downloaded from https://onlinelibrary.wiley.com/doi/10.1002/lpor.72032 by Centrum Voor Wiskunde En Info (Cwi), Wiley Online Library on [29/10/2026]. See the Terms and Conditions (https://onlinelibrary.wiley.com/terms-and-conditions) on Wiley Online Library for rules of use; OA articles are governed by the applicable Creative Commons License

in our optimization basis. This effect is clearly observed in Figure 5i,l: the theoretical relative scattered wavefronts contain steep wavefront gradients, which the experimentally optimized wavefront approximates with smooth gradients. Second, ideal time reversal of scattered wavefronts is only achieved with full vectorial complex amplitude and phase modulation capabilities. In our experimental setup, we can only shape the phase of the incident focus in Fourier space, while the amplitude remains fixed as a uniform beam profile that fills the back-focal-plane. Regions in Fourier space in which a dipole cannot efficiently radiate intensity can therefore introduce inaccuracies in the optimization result. This explains the relatively larger discrepancy between theory and experiment in Figure 5k, which we attribute to a larger mismatch between the scattered amplitude of the nanorod-on-mirror as seen in Figure 4d compared to the uniform beam profile in the experimental setup. Finally, we work in just one fixed polarization channel, which does not take polarization variations in the scattered waves into account.

5 | Angle-Resolved Extinction

From time-reversal arguments, it is expected that extinction can only happen in those regions of Fourier space in which a dipole can actually emit with non-vanishing intensity, and a strong correlation between angle-resolved extinction and dipole-scattering intensity is anticipated. We therefore investigate how the spacer-height-dependent extinction is distributed in Fourier space and compare the result to theoretically calculated scattered dipole intensities. To this end, we focus an optimum wavefront onto a cluster of 2×2 nanoparticles and measure the resulting angle-resolved reflected signal $I_{\text{cluster}}(\hat{k})$ by using Fourier microscopy (see Supporting Information for details of the full experimental setup). By recording a reference angle-resolved reflected signal in the absence of the nanoparticles $I_{\text{ref}}(\hat{k})$ (essentially the reflected signal from the back mirror only), we can derive an angle-resolved extinction pattern $E(\hat{k})$ by $E(\hat{k}) = 1 - \frac{I_{\text{cluster}}(\hat{k})}{I_{\text{ref}}(\hat{k})}$, which provides insight into the angular regions in Fourier space for which a nanoscatterer causes efficient destructive interference with the directly reflected incident field. We show such experimental angle-resolved extinction patterns in Figure 6a–e for the same selection of spacer heights as mentioned in the previous section. From these images, primarily regions of positive extinction can be discerned, sometimes approaching unity, as is the case in Figure 6a,c, which correspond to regions in Fourier space in which the nanoscatterers can fully extinguish incident radiation. A strong angle-dependent extinction efficiency is observed, which varies as a function of spacer height. We compare these angle-dependent extinction efficiencies to the calculated dipolar-scattering intensities for the exact same heights, as shown in Figure 6f–j, and observe a strong correlation between experiment and theory. This finding corroborates that the extinction of focused light is due to destructive interference of incident waves with the scattered waves of the nanoparticles, thereby providing additional evidence that the incident waves are indeed time-reversed in those regions in which a dipole is allowed to radiate. The fact that regions of non-unity extinction occur is due to the mismatch in amplitude between incident light and the dipole radiation pattern, which can be resolved only by amplitude shaping. Consequently, further amplitude shaping of the incident waves can be beneficial to reach even higher total extinction efficiencies for those spacer heights that show strong angle-dependent extinction.

An interesting follow-up question is in which channels the extinguished light is transduced. Assuming complete destructive interference between the scattered wave of the nanoparticle and the back-reflected incident wave, the incident light can be transferred into one of the following decay channels: (1) Ohmic absorption in the nanoparticle, (2) absorption in the metallic film, and (3) radiation into scattering angles larger than those collected by the microscope objective. In the Supporting Information, we have performed a theoretical analysis in which we estimate the fraction of extinguished light that is transduced into each separate decay channel by evaluating the local density of optical states (LDOS) of the dipolar particle in a stratified medium.

Finally, there are regions in Fourier space where an apparent negative extinction shows up, as we can observe, for instance, in Figure 6b,e. Negative angular extinction relates to specific regions in Fourier space in which relatively *more* light is reflected from a nanoparticle-on-mirror system than from the mirror only. This can happen in regions of the incident wavefront that are out of phase with respect to the time-reversed scattered wave of the nanoparticle, effectively leading to *constructive* interference between the scattering of the nanoparticle and the incident wave. This is, for instance, the case for the differential optimum wavefronts in Figure 5i,l. We further observe that, due to the wavefront discrepancies caused by the smooth Zernike polynomial approximation of the actually abrupt phase changes in the dipole radiation pattern, there are indeed small angular regions in which the relative optimum wavefront is slightly out of phase relative to the calculated scattered phase. These are exactly the regions that correspond to the negative extinction values of Figure 6b,e.

The central notion underlying Figure 6 is that extinction of a small object with a focused beam can be interpreted as the angle-resolved destructive interference of the reflected incident wavefront and the scattering pattern of the object. Interestingly, this also means that wavefront shaping allows one to control the regions in which extinction occurs in the back focal plane. To demonstrate this idea, we add a set of binary $0 - \pi$ phase patterns to the wavefront optimized for a 2×2 cluster of nanoparticles separated from the mirror by the optimum height of 389 nm. Since extinction is connected to the interference between the scattered field and the back-reflected incident light, one expects that, in regions where the incident phase front is toggled to be out of phase with respect to the ideal time-reversed phase front, *constructive* interference with the scattered wave occurs (i.e., *negative* extinction). The projected additional phase patterns are depicted in Figure 7a–c, which result in the corresponding angle-resolved extinction patterns shown in Figure 7d–f. We observe that negative extinction is indeed seen in those regions in which the incident wavefront is out of phase with the optimum time-reversed scattered wavefront. Effectively, the outgoing power is redirected from the positive to the negative extinction regions. In this way, angular extinction in Fourier space can be engineered by projecting additional designer patterns. In the particular case of Figure 7f, we observe that the angle-resolved extinction is drastically reduced when a $0 - \pi$ symmetric phase step is added to the optimum wavefront. Expressed in wave vector space, this particular incident wavefront is symmetry-mismatched from the

18638899, 0, Downloaded from https://onlinelibrary.wiley.com/doi/10.1002/lpor.72032 by Centrum Voor Wiskunde En Info (Cwi), Wiley Online Library on [29/10/2026]. See the Terms and Conditions (https://onlinelibrary.wiley.com/terms-and-conditions) on Wiley Online Library for rules of use; OA articles are governed by the applicable Creative Commons License

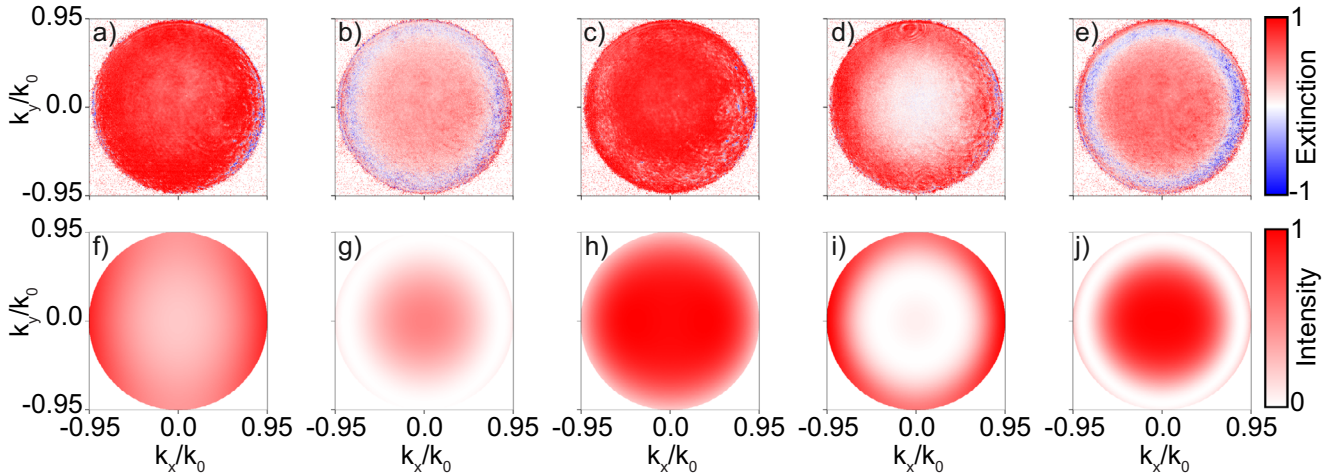


FIGURE 6 | Angle resolved extinction correlates to scattered dipole intensity. (a)–(e) Experimental angle resolved extinction patterns for optimized wavefronts illuminated onto a cluster of 2×2 nanoparticles separated from the back reflector by spacer layers of thickness (a) 202, (b) 305, (c) 389, (d) 529, and (e) 641 nm. (f)-(j) Theoretical angle resolved scattered intensity patterns of a dipole on mirror, separated by the same spacer heights as used in panels (a)–(e).

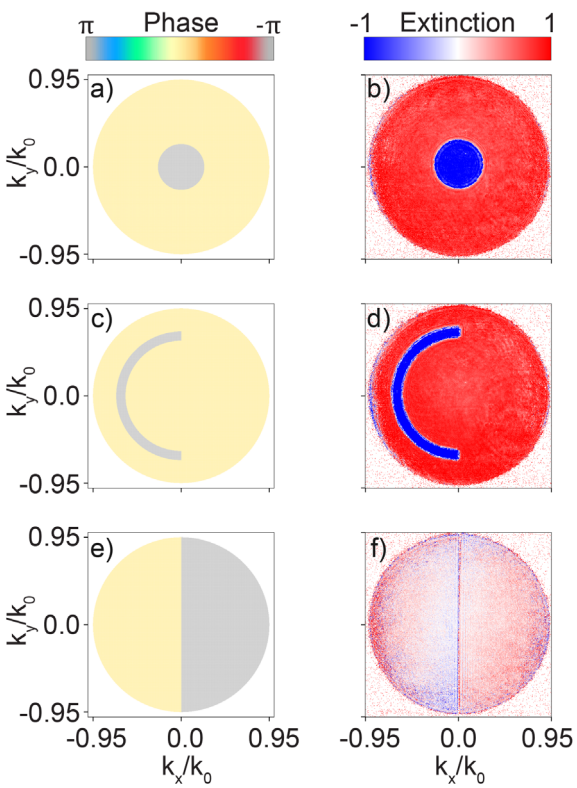


FIGURE 7 | Extinction engineering in Fourier space. Panels (a), (c), and (e) denote additional phase patterns projected on top of the optimum wavefront, and panels (b), (d), and (f) show angle-resolved extinction patterns for a 2×2 cluster of nanoparticles corresponding to these projected phase patterns. The nanoparticles are separated from the back reflector by a distance of 389 nm.

dipole mode of the particle. Expressed in real-space terms, the incident wavefront focuses to a double-lobed PSF with vanishing intensity at the center, akin to a Hermite–Gaussian beam profile, which can only interact with much weaker quadrupole terms in the particle polarizability. As the main dipolar particle resonance is not excited at all, this means that there is hardly any extinction (i.e., neither positive nor negative extinction). This observation highlights the crucial aspect of efficient generation of a scattered wave from the nanoparticle, without which no interference, and therefore no extinction, can happen. Of course, the total angle-integrated extinction cannot be lower than zero, and regions of positive and negative extinction must therefore be properly balanced. Finally, the total extinction values obtained using the non-optimal incident wavefronts of Figure 7a–c correspond to 0.44, 0.63, and 0.1, respectively. This highlights that an extinction modulation depth of at least 80% is possible through phase-only shaping.

6 | Conclusions

In summary, we study optimal extinction scenarios in finite-sized particle arrays and single-nanoparticle-based Salisbury-screen systems. We experimentally investigate how the phase of a tightly focused beam can be engineered in Fourier space for optimum extinction in single nanoparticle-on-mirror systems and qualitatively argue that the optimum incident illumination conditions are matched to the time-reversed radiation pattern of the nanoparticles. Using these tailored illumination schemes, we demonstrate that a single plasmonic nanoparticle on a reflector can attenuate 70% of a focused light beam, while a cluster of 2×2 particles can cause up to 90% extinction.

Looking ahead, higher extinction contrasts could be realized through tighter focusing using immersion optics. Additionally, incorporating amplitude and polarization [35] structuring capabilities in our wavefront shaping setup could further enhance mode matching with the scatterer's radiation pattern. On the side of the scatterer, higher extinction cross sections could be engineered by mixing multipole contributions in low-loss dielectric particles supporting Mie resonances [21, 36, 37]. Besides reaching optimum extinction, the developed framework could also be exploited to *probe* multipole resonances in scattering objects by analyzing the optimum wavefront and corresponding

18638899, 0, Downloaded from https://onlinelibrary.wiley.com/doi/10.1002/lpor.72032 by Centrum Voor Wiskunde En Info (Cwi), Wiley Online Library on [29/10/2026]. See the Terms and Conditions (https://onlinelibrary.wiley.com/terms-and-conditions) on Wiley Online Library for rules of use; OA articles are governed by the applicable Creative Commons License

angle-resolved extinction. This could be potentially interesting in, for instance, Fano-resonant systems [38, 39], where precise identification of dominant modes is critical. Additionally, the investigated platform could be exploited as a highly responsive optical sensor, where one could investigate how perturbations on the nanoscale [40] influence optimum extinction conditions. Finally, an interesting continuation to this work would be to experimentally probe the specific channels into which the extinguished light is transduced (i.e., absorption at the particles, launching of propagating surface modes, and direct inelastic absorption at the surface). Experimentally, propagating surface modes could be visualized by, for instance, electron beams [41], or scanning near-field probes [42], while many photothermal schemes [43] are available to probe particle absorption. Altogether, our work highlights the potential of tailored wavefront engineering to maximize optical extinction at the nanoscale, paving the way for ultracompact light control.

7 | Methods

7.1 | Sample Fabrication

We fabricate the nanoscatterers-on-mirror samples by electron beam (e-beam) lithography using the following procedure. A 170 μm-thick glass substrate (Menzel–Gläser) is sonicated for 10 min in H_2O and cleaned in a solution of base piranha (NH_4OH:H_2H_2:H_2O = 1:1:5) at 75°C for 15 min. After thoroughly rinsing excess piranha with H_2O, the sample is blown dry with N_2. For high-resolution patterning of nanostructures, we utilize a multistack thin film recipe consisting of a thick polymethyl methacrylate (PMMA) bottom layer, followed by a thin Ge layer, which is finally covered by a thin e-beam resist (CSAR AR-P 6200:09) as top layer. Here, the thin e-beam resist allows for high resolution e-beam writing, the Ge layer serves as a sacrificial mask through which the patterns can be etched, and the thick PMMA layer generates sufficient undercut for lift-off. We start by spin-coating a solution of (PMMA:Anisole = 3:2) at 3000 rpm for 45 s, followed by baking the sample at 180°C for 2 min, resulting in a 150 nm layer of PMMA, after which a 20 nm Ge mask is deposited by thermal evaporation (Polyteknik Flextura M508 E) at a rate of 0.05 nm/s. A solution of e-beam resist (CSAR:Anisole = 3:2) is then spin-coated at 4000 rpm for 60 s and baked at 150°C for 2 min, resulting in a 60 nm resist layer. Then, 50 nm gold nanoparticles are drop-cast in the corners of the substrate for e-beam alignment purposes. E-beam exposure (Raith) is done at an acceleration voltage of 50 kV, a beam current of 0.123 nA, and a nominal dose of 130 μC/cm^2. After exposure, the sample is developed in consecutive solutions of (1) amyl-acetate for 60 s, (2) o-xylene for 6 s, (3) methyl-isobutyl-ketone/2-propanol (MIBK:IPA = 9:1) for 15 s, (4) 2-propanol (IPA) for 30 s, and finally blown dry with N_2. We then plasma etch (Oxford Plasmalab 80+) the pattern through the Ge mask using a gas mixture of O_2:SF_6 = 1:5 for 60 s at a forward power of 30 W, and the PMMA layer using O_2 plasma for 100 s at forward power of 50 W. After etching, we deposit a 40 nm gold film using e-beam evaporation (Polyteknik Flextura M508 E) at a rate of 0.05 nm/s. Excess PMMA, Ge and gold are removed by a lift-off process by immersing the sample in acetone at 50°C for 3 h, followed by gentle flushing. After characterization of the nanoparticle sample with an SEM, we spin-coated a solution of commercial spin-on glass (Microresist OrmoComp) at 4000 rpm for 60 s and baked at 100°C for 1 min, resulting in a thin film of 50 nm. This thin film smooths possible surface modulations caused by the nanoparticles before deposition of the dielectric graded layer. To obtain a variable spacer height, we deposit SiO_2 at a rate of 0.1 nm/s using e-beam evaporation (Polyteknik Flextura M508 E). A linear shutter that is partly covering the sample can be controlled to obtain a staircase-like thin film that is increasing in thickness with steps of roughly 10 nm, with a lateral step size of 500 μm. Finally, a 50 nm gold back reflector is deposited by e-beam evaporation at a rate of 0.05 nm/s.

7.2 | Theoretical Calculations

Nanoscatterer-on-mirror emission patterns are calculated using the Green function formalism. In brief, we model the scatterers as electric dipole sources $\mathbf{p}$ positioned at $\mathbf{r}_0$ above a back reflector. For such systems, the total Green function $\overleftrightarrow{\mathbf{G}}(\mathbf{r}_1, \mathbf{r}_0)$ can be separated into free-space and reflected contributions [34], after which the scattered electric fields $\mathbf{E}$ can be determined in the reflected far-field half-space at position $\mathbf{r}_1$ as

$$\mathbf{E}(\mathbf{r}_1, \mathbf{r}_0) = \omega^2 \mu_0 \overleftrightarrow{\mathbf{G}}(\mathbf{r}_1, \mathbf{r}_0) \cdot \mathbf{p}, \tag{3}$$

where ω is the driving frequency and μ_0 the free-space permeability. We construct the layered medium in the calculations to precisely mimic the experimental conditions. The consecutive layers are: (1) a semi-infinite half-space of air with a refractive index $n_{\text{air}} = 1$, (2) a 50 nm gold back reflector with refractive index taken from Ref. [44], (3) the variable spacer layer of SiO_2 with $n_{SiO_2} = 1.42$, and (4) a semi-infinite layer of glass with $n_{\text{glass}} = 1.5$. The dipole scatterer is positioned above the back reflector according to the experimental parameters, and the dipole emission is collected on the glass side.

Acknowledgments

This work is part of the Dutch Research Council (NWO) and was performed at the research institutes ARCNL and AMOLF. The Advanced Research Center for Nanolithography ARCNL is a public–private partnership between the University of Amsterdam, Vrije Universiteit Amsterdam, Rijksuniversiteit Groningen (RUG), the Netherlands Organization for Scientific Research (NWO), and the semiconductor-equipment manufacturer ASML. F.J.G.A. acknowledges funding from ERC (101141220-QUEFES) and the Catalan CERCA Program.

Funding

The work was funded by the Advanced Research Center for Nanolithography, a public-private partnership between the University of Amsterdam, Vrije Universiteit Amsterdam, University of Groningen, the Netherlands Organization for Scientific Research (NWO), and the semiconductor equipment manufacturer ASML. F.J.G.A. acknowledges funding from ERC (101141220-QUEFES) and the Catalan CERCA Program.

Conflicts of Interest

The authors declare no conflicts of interest.

18638899, 0, Downloaded from https://onlinelibrary.wiley.com/doi/10.1002/lpor.72032 by Centrum Voor Wiskunde En Info (Cwi), Wiley Online Library on [29/10/2026]. See the Terms and Conditions (https://onlinelibrary.wiley.com/terms-and-conditions) on Wiley Online Library for rules of use; OA articles are governed by the applicable Creative Commons License

Data Availability Statement

The data that support the findings of this study are available from the corresponding author upon reasonable request.

References

1. K. Catchpole and A. Polman, "Plasmonic Solar Cells," *Optics Express* 16, no. 26 (2008): 21793–21800.

2. J. N. Anker, W. P. Hall, O. Lyandres, N. C. Shah, J. Zhao, and R. P. Van Duyne, "Biosensing With Plasmonic Nanosensors," *Nature Materials* 7, no. 6 (2008): 442–453.

3. G. T. Reed, G. Mashanovich, F. Y. Gardes, and D. J. Thomson, "Silicon Optical Modulators," *Nature Photonics* 4, no. 8 (2010): 518–526.

4. T.-K. Wu, "Frequency Selective Surfaces," in *Encyclopedia RF Microwave Engineering* (Wiley, 2005): 1–7.

5. W. W. Salisbury, "Absorbent Body for Electromagnetic Waves," (June 10, 1952) US Patent 2,599,944.

6. R. L. Fante and M. T. McCormack, "Reflection Properties of the Salisbury Screen," *IEEE Transactions on Antennas and Propagation* 36, no. 10 (1988): 1443–1454.

7. N. I. Landy, S. Sajuyigbe, J. J. Mock, D. R. Smith, and W. J. Padilla, "Perfect Metamaterial Absorber," *Physical Review Letters* 100, no. 20 (2008): 207402.

8. C. M. Watts, X. Liu, and W. J. Padilla, "Metamaterial Electromagnetic Wave Absorbers," *Advanced Materials* 24, no. 23 (2012): OP98–OP120.

9. N. Liu, M. Mesch, T. Weiss, M. Hentschel, and H. Giessen, "Infrared Perfect Absorber and Its Application as Plasmonic Sensor," *Nano Letters* 10, no. 7 (2010): 2342–2348.

10. Y. Avitzour, Y. A. Urzhumov, and G. Shvets, "Wide-Angle Infrared Absorber Based on a Negative-Index Plasmonic Metamaterial," *Physical Review B* 79, no. 4 (2009): 045131.

11. M. Pu, C. Hu, M. Wang, et al., "Design Principles for Infrared Wide-Angle Perfect Absorber Based on Plasmonic Structure," *Optics Express* 19, no. 18 (2011): 17413–17420.

12. S. Thongrattanasiri, F. H. L. Koppens, and F. J. García de Abajo, "Complete Optical Absorption in Periodically Patterned Graphene," *Physical Review Letters* 108, no. 4 (2012): 047401.

13. K. Aydin, V. E. Ferry, R. M. Briggs, and H. A. Atwater, "Broadband Polarization-Independent Resonant Light Absorption Using Ultrathin Plasmonic Super Absorbers," *Nature Communications* 2, no. 1 (2011): 517.

14. C. Hu, Z. Zhao, X. Chen, and X. Luo, "Realizing Near-Perfect Absorption at Visible Frequencies," *Optics Express* 17, no. 13 (2009): 11039–11044.

15. A. Berkhout and A. F. Koenderink, "Perfect Absorption and Phase Singularities in Plasmon Antenna Array Etalons," *ACS Photonics* 6, no. 11 (2019): 2917–2925.

16. W. Wan, Y. Chong, L. Ge, H. Noh, A. D. Stone, and H. Cao, "Time-Reversed Lasing and Interferometric Control of Absorption," *Science* 331, no. 6019 (2011): 889–892.

17. Y. D. Chong, L. Ge, H. Cao, and A. D. Stone, "Coherent Perfect Absorbers: Time-Reversed Lasers," *Physical Review Letters* 105, no. 5 (2010): 053901.

18. S. Tretyakov, "Maximizing Absorption and Scattering by Dipole Particles," *Plasmonics* 9, no. 4 (2014): 935–944.

19. R. Alaee, M. Albooyeh, and C. Rockstuhl, "Theory of Metasurface Based Perfect Absorbers," *Journal of Physics D: Applied Physics* 50, no. 50 (2017): 503002.

20. V. Grigoriev, N. Bonod, J. Wenger, and B. Stout, "Optimizing Nanoparticle Designs for Ideal Absorption of Light," *ACS Photonics* 2, no. 2 (2015): 263–270.

21. Z. Ruan and S. Fan, "Superscattering of Light From Subwavelength Nanostructures," *Physical Review Letters* 105, no. 1 (2010): 013901.

22. G. Zumofen, N. M. Mojarad, V. Sandoghdar, and M. Agio, "Perfect Reflection of Light by an Oscillating Dipole," *Physical Review Letters* 101, no. 18 (2008): 180404.

23. I. Gerhardt, G. Wrigge, P. Bushev, et al., "Strong Extinction of a Laser Beam by a Single Molecule," *Physical Review Letters* 98, no. 3 (2007): 033601.

24. J. Zirkelbach, B. Gmeiner, J. Renger, et al., "Partial Cloaking of a Gold Particle by a Single Molecule," *Physical Review Letters* 125, no. 10 (2020): 103603.

25. A. N. Vamivakas, M. Atatüre, J. Dreiser, et al., "Strong Extinction of a Far-Field Laser Beam by a Single Quantum Dot," *Nano Letters* 7, no. 9 (2007): 2892–2896.

26. S. J. van Enk and H. Kimble, "Strongly Focused Light Beams Interacting With Single Atoms in Free Space," *Physical Review A* 63, no. 2 (2001): 023809.

27. M. Stobińska, G. Alber, and G. Leuchs, "Perfect Excitation of a Matter Qubit by a Single Photon in Free Space," *Europhysics Letters* 86, no. 1 (2009): 14007.

28. E. J. C. Dias and F. J. García de Abajo, "Complete Coupling of Focused Light to Surface Polaritons," *Optica* 8, no. 4 (2021): 520–531.

29. A. Proskurin, A. Bogdanov, and D. G. Baranov, "Perfect Absorption of a Focused Light Beam by a Single Nanoparticle," *Laser & Photonics Reviews* 15, no. 8 (2021): 2000430.

30. I. M. Vellekoop and A. P. Mosk, "Focusing Coherent Light Through Opaque Strongly Scattering Media," *Optics Letters* 32, no. 16 (2007): 2309–2311.

31. V. Lakshminarayanan and A. Fleck, "Zernike Polynomials: A Guide," *Journal of Modern Optics* 58, no. 7 (2011): 545–561.

32. E. Goi, S. Schoenhardt, and M. Gu, "Direct Retrieval of Zernike-Based Pupil Functions Using Integrated Diffractive Deep Neural Networks," *Nature Communications* 13, no. 1 (2022): 7531.

33. L. Miccio, D. Alfieri, S. Grilli, et al., "Direct Full Compensation of the Aberrations in Quantitative Phase Microscopy of Thin Objects by a Single Digital Hologram," *Applied Physics Letters* 90, no. 4 (2007): 041104.

34. L. Novotny and B. Hecht, *Principles of Nano-Optics* (Cambridge University Press, 2012).

35. A. Rubano, F. Cardano, B. Piccirillo, and L. Marrucci, "Q-Plate Technology: A Progress Review," *Journal of the Optical Society of America B* 36, no. 5 (May 2019): D70–D87, https://doi.org/10.1364/JOSAB.36.000D70.

36. M. V. Rybin, K. L. Koshelev, Z. F. Sadrieva, et al., "High-Q Supercavity Modes in Subwavelength Dielectric Resonators," *Physical Review Letters* 119, no. 24 (2017): 243901.

37. A. I. Kuznetsov, A. E. Miroshnichenko, M. L. Brongersma, Y. S. Kivshar, and B. Luk'yanchuk, "Optically Resonant Dielectric Nanostructures," *Science* 354, no. 6314 (2016): aag2472.

38. M. Hentschel, D. Dregely, R. Vogelgesang, H. Giessen, and N. Liu, "Plasmonic Oligomers: The Role of Individual Particles in Collective Behavior," *ACS Nano* 5, no. 3 (2011): 2042–2050.

39. N. Verellen, Y. Sonnefraud, H. Sobhani, et al., "Fano Resonances in Individual Coherent Plasmonic Nanocavities," *Nano Letters* 9, no. 4 (2009): 1663–1667.

40. P. Zijlstra, P. M. R. Paulo, and M. Orrit, "Optical Detection of Single Non-Absorbing Molecules Using the Surface Plasmon Resonance of a Gold Nanorod," *Nature Nanotechnology* 7, no. 6 (2012): 379–382.

41. X. Li, G. Haberfehlner, U. Hohenester, O. Stéphan, G. Kothleitner, and M. Kociak, "Three-Dimensional Vectorial Imaging of Surface Phonon Polaritons," *Science* 371, no. 6536 (2021): 1364–1367.

42. A. V. Zayats, I. I. Smolyaninov, and A. A. Maradudin, "Nano-Optics of Surface Plasmon Polaritons," *Physics Reports* 408, no. 3–4 (2005): 131–314.

18638899, 0, Downloaded from https://onlinelibrary.wiley.com/doi/10.1002/lpor.72032 by Centrum Voor Wiskunde En Info (Cwi), Wiley Online Library on [29/10/2026]. See the Terms and Conditions (https://onlinelibrary.wiley.com/terms-and-conditions) on Wiley Online Library for rules of use; OA articles are governed by the applicable Creative Commons License

43. S. Adhikari, P. Spaeth, A. Kar, M. D. Baaske, S. Khatua, and M. Orrit, "Photothermal Microscopy: Imaging the Optical Absorption of Single Nanoparticles and Single Molecules," *ACS Nano* 14, no. 12 (2020): 16414–16445.

44. G. Rosenblatt, B. Simkhovich, G. Bartal, and M. Orenstein, "Nonmodal Plasmonics: Controlling the Forced Optical Response of Nanostructures," *Physical Review X* 10, no. 1 (2020): 011071.

Supporting Information

Additional supporting information can be found online in the Supporting Information section.

Supporting File: lpor72032-sup-0001-SuppMat.pdf.

18638899, 0, Downloaded from https://onlinelibrary.wiley.com/doi/10.1002/lpor.72032 by Centrum Voor Wiskunde En Info (Cwi), Wiley Online Library on [29/10/2026]. See the Terms and Conditions (https://onlinelibrary.wiley.com/terms-and-conditions) on Wiley Online Library for rules of use; OA articles are governed by the applicable Creative Commons License